Effect of vacuum pressure on small crack propagation in Ti-6Al-4V

Fumiyoshi Yoshinaka[1], Gaoge Xue[2], Nao Fujimura[2], Takashi Nakamura[2,*]

[1] National Institute for Materials Science, 1-2-1 Sengen, Tsukuba, Ibaraki 305-0047, Japan

[2] Division of Mechanical and Space Engineering, Hokkaido University, Sapporo, Hokkaido 060-8628, Japan

[*]Corresponding author:

Email: nakamut@eng.hokudai.ac.jp

Phone: +81-11-706-6419

Abstract

In this study, small crack propagation tests are conducted on artificially defected specimens of Ti-6Al-4V under air and vacuum pressures of 10^{0} Pa, 10^{-2} Pa, 10^{-4} Pa, and 10^{-6} Pa. Fracture surfaces between these environments are compared, and the effect of vacuum pressure on the crack propagation process is investigated. The similarities between surface cracks in vacuum and internal cracks in the very high cycle regime are also discussed from the perspectives of crack propagation rate and fractographic characteristics. From the results, it was observed that there was a tendency for the crack initiation life to increase and the crack propagation rate to decrease with a decrease in the vacuum pressure, although no notable distinction was observed in air and under 10^{0} Pa. The fractography exhibited an angular surface with sharp edges in air and under 10^{0} Pa. However, a granular feature with rounded edges was observed below 10^{-2} Pa and became more pronounced as the vacuum pressure decreased. The window periods, which formed an oxidized surface coverage, were believed to account for the vacuum effect on crack propagation rate and fracture surface features. Both the crack propagation rate and fractographic features of surface cracks

under 10^{-4}–10^{-6} Pa resembled those of internal cracks; therefore, the presumably working vacuum environment around internal cracks was considered to be at a high vacuum level.

Key Words: Very high cycle fatigue, Vacuum, Fractography, Internal crack, Synchrotron radiation

1. Introduction

Ti-6Al-4V alloy is one of the most widely used materials in aerospace industries owing to its remarkable mechanical properties, such as its excellent specific strength, heat corrosion, and fatigue properties. However, it has been confirmed that fatigue fractures still occur in many metal materials when the applied stress is below the conventional fatigue limit [1-2]. In addition, in titanium alloys, the fracture mode transfers from the surface-originating fractures to interior-originating fractures when the number of loading cycles reaches the very high cycle fatigue (VHCF) regime [3-12]. This particular feature indicates that it is necessary to investigate the internal crack behavior in order to better understand the VHCF mechanism.

One of the differences between surface cracks and internal cracks is that unlike surface cracks that are exposed to the air, the environment surrounding internal crack is more similar to a vacuum-like environment, which means that gas adsorption and oxidation effects do not occur during crack propagation [13, 14]. The present authors have investigated the effect of a vacuum environment on the crack propagation of high-strength steels and titanium alloys [15-18]. On the basis of the results, the behaviors of surface fracture under vacuum, such as the crack propagation rate and fracture surface features, were found to have characteristics very similar to those of internal fractures. These phenomena show that it is acceptable to clarify the internal fracture mechanism by means of simulating surface

fractures in a vacuum. In particular, in Ti-6Al-4V, the crack growth behaviors of long and short cracks were investigated in high vacuum (10^{-6} Pa) and air conditions [16, 17]. The results showed that regardless of the initial crack length, the crack propagation rate was much lower in the high vacuum environment than in air. Moreover, fracture surface similarities were also observed between surface cracks in a high vacuum and internal cracks.

The slow crack growth in vacuum environment has been previously reported by other researchers [19, 20]. Some of the earlier studies, which were conducted primarily around the time of the Space Race, provided important results that the fatigue life of some alloys increased with decreasing vacuum pressure [21, 22]. Gao et al. reported that on A7075 alloys, the crack propagation rate was sensitive to the variations in vacuum pressure [23]. Therefore, it is not reasonable to summarize all vacuum conditions using only the word “vacuum”, and it is necessary to investigate the crack growth behavior for various vacuum pressures. Because of the difficulty associated with measuring precisely the pressure around internal cracks, it is important to focus on the crack propagation behavior under various vacuum pressure conditions in order to simulate accurately internal cracks, and to help us to understand further the internal crack mechanism. In this study, fatigue crack propagation experiments of Ti-6Al-4V were conducted to investigate the effect of vacuum pressure on small crack propagation behavior by using hour-glass shape specimens with an artificial defect. In order to compare the results with our previous data, which were obtained under 10^{-6} Pa [16], the experimental environments chosen were air, and pressures of 10^{0} Pa, 10^{-2} Pa, and 10^{-4} Pa. Then, to enable a more detailed comparison of the experiments, fractography was employed for the analysis of the fracture surface.

2. Experimental procedures

2.1 Material and specimens

The applied material was an (α+β) titanium alloy, and its chemical composition is listed in **Table 1**. The as-received material was a 20-mm-diameter bar with heat treatment involving the following processes: solution treatment at 1203 K for 3.6 ks, after which it proceeded to the aging process at 978 K for 7.2 ks, followed by air cooling. The (α+β) dual-phase microstructure and mechanical properties are shown in **Fig. 1** and **Table 2**, respectively. The average grain size was about 10 μm for each phase [17]. The hourglass shape with a $\emptyset 4 \times 6$ mm straight section was chosen for the specimen configuration, as shown in **Fig. 2**. The specimens were fabricated from the heat-treated bars via lathe machining and were polished with emery paper until #2000. Then, they were buffed with diamond abrasive to obtain a mirror surface.

Table 1 Chemical compositions of Ti-6Al-4V. (mass%)

Al	V	O	N	C	Fe	H	Ti
6.12	**4.27**	**0.16**	**0.002**	**0.02**	**0.15**	**0.0029**	**Bal.**

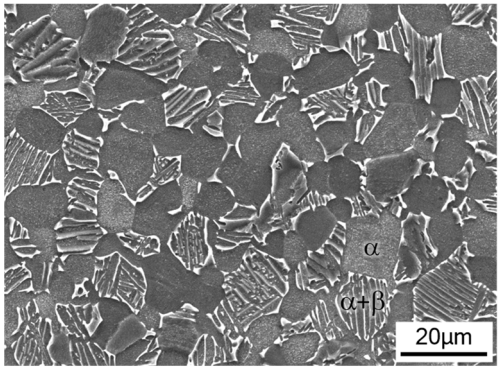

Fig. 1 Microstructure of Ti-6Al-4V.

Table 2 Mechanical properties after the heat treatment.

Tensile strength [MPa]	0.2% proof stress [MPa]	Elongation (%)	Reduction of area (%)	Hardness (Hv)
943	**860**	**17**	**40**	**316**

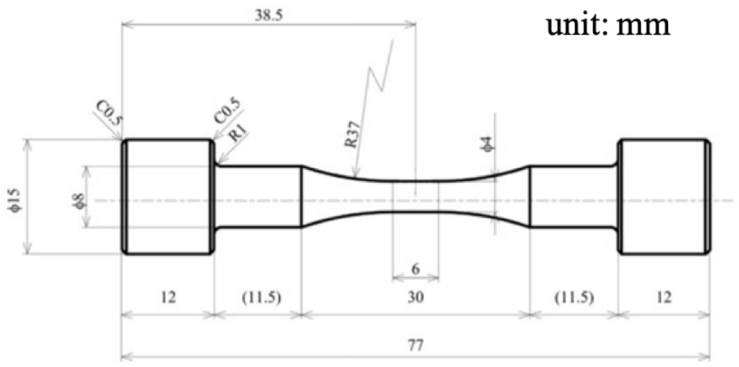

Fig. 2 Shape and dimension of specimen.

As a crack started, an artificial surface defect was introduced at the center of the straight section. It has been reported that the internal fatigue crack of Ti-6Al-4V occurs from the α-phase formed facet with a size similar to the average α grain size [24]. In our previous research, we employed an excimer laser to create an artificial defect with a cylinder shape having a diameter of Ø30 μm [16]. In this study, a picosecond laser characterized by its negligible heat accumulation due to its short-pulse duration, was used to create a defect with a lower size. The size of this artificial defect was closer to the actual facet size and more convenient for investigating the crack propagation rate at a lower ΔK. **Fig. 3 a** and **b** show the image of the small defect on the fracture surface and the specimen surface, respectively. As shown in **Fig. 3 a**, the fatigue crack initiated from the artificial defect, which showed a cone-like shape with a depth of around 15 μm. To enable the crack to propagate perpendicular to the loading direction more naturally, we designed the bottom of the cone to have an elliptic shape, as shown in **Fig. 3 b**. The lengths of the major axis and minor axis were 20 μm and 10 μm, respectively.

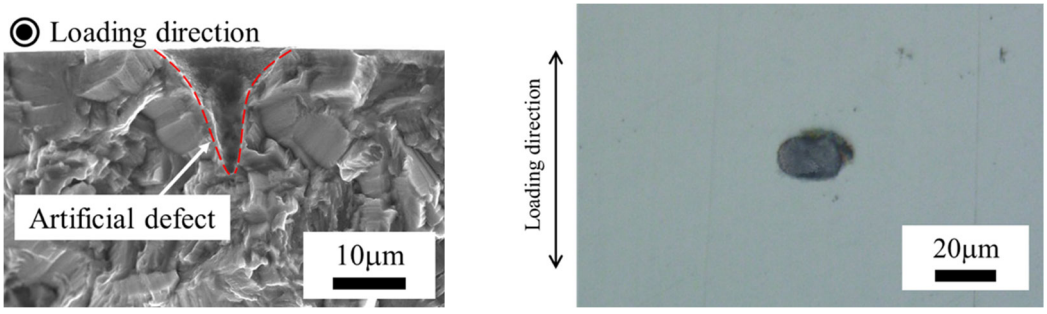

a. Shape on the fracture surface. b. Shape on the specimen surface.

Fig. 3 Configuration of the small defect.

2.2 Experimental procedure

The crack propagation tests were conducted by the ΔK-increasing test under a constant load amplitude. The vacuum fatigue testing machine developed in our laboratory [17] was used to carry out fatigue tests in various vacuum environments, as will be mentioned later. A dry scroll pump and a turbo-molecular pump work concurrently to evacuate the gas in the vacuum chamber. In order to observe the crack length and the crack propagation behavior during the fatigue test, we equipped the vacuum chamber with a viewport. A digital microscope with a high spatial resolution of submicron order (Keyence VHX-2000) was utilized to capture the image in the vacuum chamber through the viewport.

The tests were carried out under sinusoidal waveform loading at a stress ratio of 0.1 and a frequency of 60 Hz. The fatigue limit for surface fracture is approximately 725 MPa under a stress ratio of 0.1 [3], and the applied maximum stress was selected as 800 MPa. The test environments were air, 10^{0} Pa, 10^{-2} Pa, and 10^{-4} Pa under 25 °C. The fatigue test was suspended after specific cycles in order to acquire images of the cracks. The crack length $2c$ was defined as the length between two crack tips on the specimen surface projected to the plane perpendicular to the loading direction. Both the crack length and the current cycles were recorded during the observations. For a clear investigation of the crack feature, a tensile load corresponding to 80% of the maximum stress of crack growth tests was applied to the specimen during the observation to open the crack. After the specimen fractured, fractography was conducted via scanning electron microscopy (SEM) (Keyence VE-9800) to compare the fracture surfaces between various test environments.

2.3 Calculation of the stress intensity factor range

The crack propagation rate in each environment against the stress intensity factor range was measured to simply compare their crack growth behaviors. The crack propagation rate was defined as the crack propagation length per cycle, as calculated by the average crack propagation rate between two measuring points. **Fig. 4** shows the example of the fracture surface originating from the artificial defect and **Fig. 5** depicts the schematic of the crack shape that propagated from an artificial defect. The measured crack length c and the distance from the artificial defect to the crack front a were assumed to be equal (c=a) in the present work as explained later. To describe the behavior at the crack front, a was converted from the measured length c in order to calculate the propagation rate da/dN. The stress intensity factor ΔK at the crack front was calculated using **Eq.** (1) [25].

$$\Delta K = F_1 \Delta\sigma\sqrt{\pi a}, \quad (1)$$

where F_1 is a factor related to the aspect ratio in terms of the crack geometry a/c and the ratio of the crack depth to the specimen radius a/r. As mentioned above, in the calculation, the aspect ratio a/c was set to 1. In this case, the F_1 value is as shown in **Table 3** based on a/r, and the linear interpolation was applied to the calculation according to each crack length. Crack propagation in the c direction is mechanically easier than that in the a direction, especially for a small crack regime. Therefore, the assumption of a semi-circular crack shape may lead to the overestimation of ΔK, especially at the early stage of crack growth. The present work assumed that the crack propagated in a semi-circular shape to simply compare the results obtained in each environment because it was almost impossible to identify the actual crack shape via specimen surface observation.

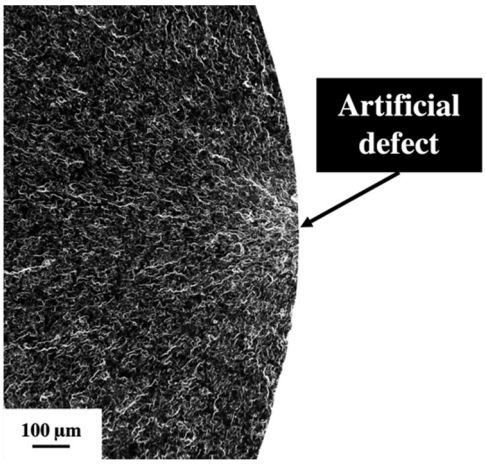

Fig. 4 Example of the semi-circular crack shape on the fracture surface (in air).

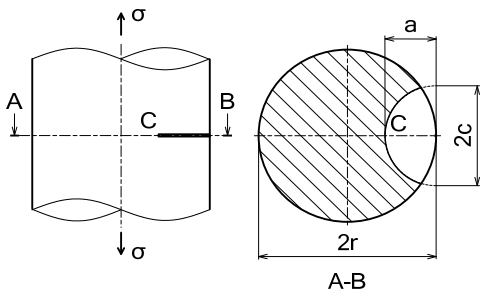

Fig. 5 Schematic of crack shape on fracture surface.

Table 3 Relation between a/r value and correction factor F_1 [25].

a/r	0	0.125	0.250	0.375	0.500
F_1	0.660	0.665	0.683	0.714	0.758

3. Crack propagation behavior

3.1 Relation between crack length and number of cycles

According to the observation results, the crack initiated from the artificial defect, and was propagated, leading to final fracture under air, 10^0 Pa, and the 10^{-2} Pa environment. However, although the artificial defects were also activated to generate cracks under the 10^{-4} Pa environment, these cracks did not evolve to the main cracks, and the specimens were fractured from within. **Fig. 6** and **Table 4** show the relationships between the measured crack length $2c$ and the number of cycles N. Our previous results obtained with respect to excimer-laser defects under 10^{-6} Pa are also included [16].

The number of cycles to crack initiation N_i was determined as the number of cycles when a crack that propagated from the artificial defect was first detected. The crack lengths at N_i varied from 20–50 μm. Because of the different types of artificial defects, the N_i value of 10^{-6} Pa will not be discussed. Overall, N_i generally increased with a decrease of the vacuum pressure. In the case of air, 10^0 Pa, and

10^{-2} Pa, N_i had a similar order of magnitude, but was slightly developed in 10^{-2} Pa. In contract, N_i increased in 10^{-4} Pa by almost seven times more than that in air and 10^{0} Pa. From the perspective of the tendency in the early crack propagation stage, the curves between air and 10^{0} Pa as well as those between 10^{-4} Pa and 10^{-6} Pa did not show pronounced differences. Similar results that the decrease of vacuum pressure increased the crack initiation life and fatigue life have been reported in other studies [12, 26, 27].

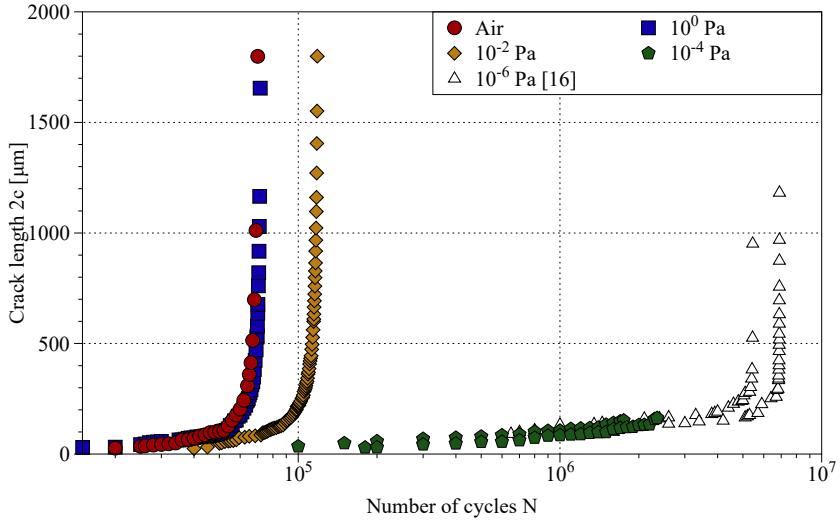

Fig. 6 Relation between crack length 2c and number of cycles N.

Table 4 Crack initiation and fatigue behaviors under different environments.

Test environment	Number of cycles to crack initiation N_i	Number of cycles to failure N_f	Main crack origin site
Air	2.0×10^4	7.0×10^4	Small defect
10^0 Pa	1.5×10^4	7.2×10^4	Small defect
10^{-2} Pa	4.0×10^4	1.2×10^5	Small defect
10^{-4} Pa	1.0×10^5	1.8×10^6	Interior
	1.8×10^5	2.4×10^6	Interior
10^{-6} Pa [16]	–	5.5×10^6	Small defect
	–	6.9×10^6	Small defect

3.2 Crack propagation rate

3.2.1 $da/dN - \Delta K$ in air and 10^0 Pa

Fig. 7 shows plots of the relations between *da*/*dN* and Δ*K* in air and 10^0 Pa environments. The LOESS fitting curves were also applied for air with a solid line and 10^0 Pa with a dashed line. There is no clear difference in the two sets of data. In other words, the vacuum effect on the crack propagation process is not pronounced under a pressure of 10^0 Pa. In the case of 10^0 Pa, the slowest crack propagation rate below around 8 MPa√m (low Δ*K* regime) was reached at around 10^{-10} m/cycles, which was slightly less than what was obtained for air. Then, the crack propagation rate increased linearly with an increasing Δ*K*.

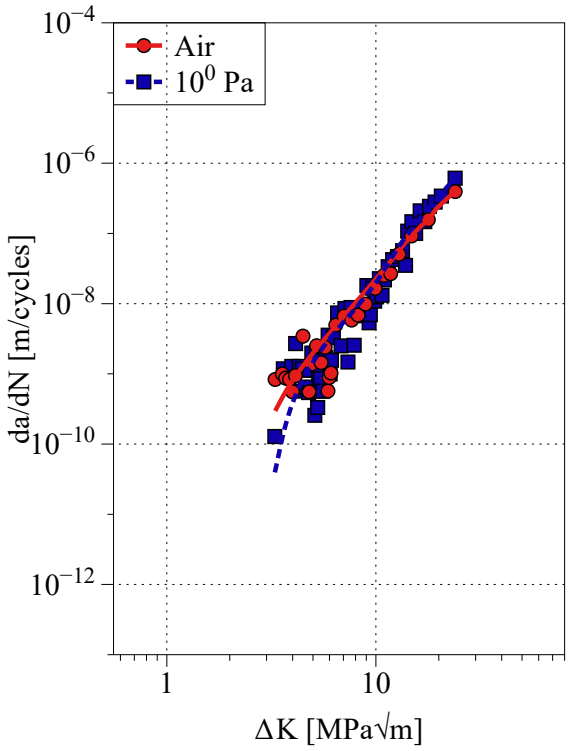

Fig. 7 Comparison between *da*/*dN* and Δ*K* in air and 10^0 Pa.

3.2.2 *da*/*dN* – Δ*K* in air and all vacuum conditions

Fig. 8 shows the relations between *da*/*dN* and Δ*K* under all test conditions. The results in air and 10^0 Pa are only shown with the LOESS fitting curve. Our previous results in 10^{-6} Pa [16] are also plotted in the figure using hollow triangle marks.

For 10^{-2} Pa, the crack propagation rate was slightly less than that in air and 10^{0} Pa, but it was higher than that in 10^{-4} Pa at the same ΔK which indicates that the effect of the vacuum on the crack growth emerged where the vacuum pressure was lower than or equaled to 10^{-2} Pa. The deviation in the propagation rate was pronounced in the low ΔK regime below approximately 8 MPa√m. However, in the high ΔK regime, the deviation became smaller and the crack propagation rate increased linearly with increasing ΔK.

In the case of 10^{-4} Pa, the crack propagation rate in the high ΔK regime over around 8 MPa√m could not be obtained because the crack from the artificial defect did not develop to the main crack, and the fracture was internal. Nearly 80% of the crack propagation rate data in the 10^{-4} Pa environment was under 10^{-10} m/cycles. The lattice spacing of Ti-6Al-4V is around 10^{-10} m, and this result therefore means that the crack in 10^{-4} Pa could not propagate continuously. This intermittent crack behavior has also been reported in other studies [28, 29]. In other words, the 10^{-4} Pa environment had a more pronounced vacuum effect on the crack propagation process. In addition, the similarity of the crack propagation rate in the low ΔK regime can be clearly observed between 10^{-4} Pa and 10^{-6} Pa. In conclusion, comparing the data between 10^{-2} Pa, 10^{-4} Pa, and 10^{-6} Pa, the crack propagation rate decreased with a decrease of vacuum pressure, especially in the low ΔK regime. Similarly, in the high ΔK regime, the propagation rate at 10^{-6} Pa is less than that in 10^{-2} Pa, but the difference was not as pronounced as that in the low ΔK regime lower than around 8 MPa√m.

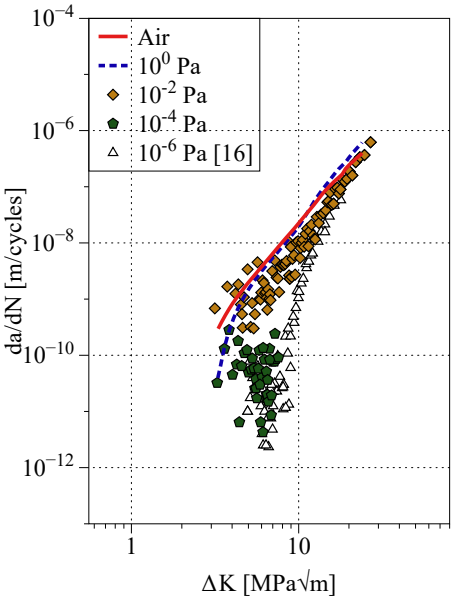

Fig. 8 Comparison between da/dN and ΔK for all test vacuum conditions.

4. Fractography

Fig. 9 shows the schematic of the crack propagation process in this study. The crack propagation process is generally classified into three stages: Stage I, Stage II, and Stage III [30-32]. In Ti-6Al-4V, Stage I is the crack initiation process corresponding to the facet formation. Stage II can be further subdivided into Stage II-a, Stage II-b, and Stage II-c, where Stage II-a is the region that is sensitive to the microstructure. Stage II-b is the region following the crack linear propagation law [33, 34]. In the present study, the crack was activated by an artificial defect instead of the facet, which means that Stage I did not exist, and Stage II-a commenced from the vicinity of the artificial defect. In the latter part of this section, the characteristics of fracture surfaces are discussed with regard to various vacuum pressures.

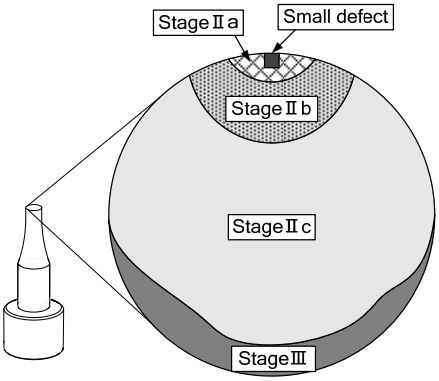

Fig. 9 Schematic of fracture surface.

4.1 Fracture surfaces at low magnification

Fig. 10 shows the SEM images of fracture surfaces in various environments. Regardless of the environment, we can observe a bright and rough texture with a radial pattern near the artificial defect, corresponding to a low ΔK regime. After the crack propagates into the high ΔK regime, the fracture surface becomes dark and shows a flat and smooth texture. A similar pattern was also reported in our previous research [16]. These dissimilar textures were considered to represent Stage II-a and Stage II-b.

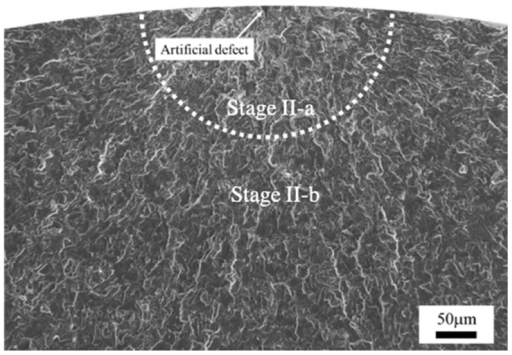

a. Air

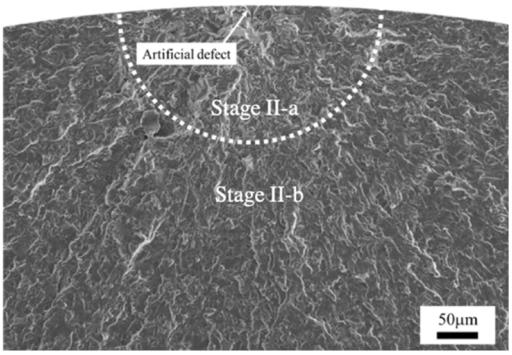

b. 10^{0} Pa

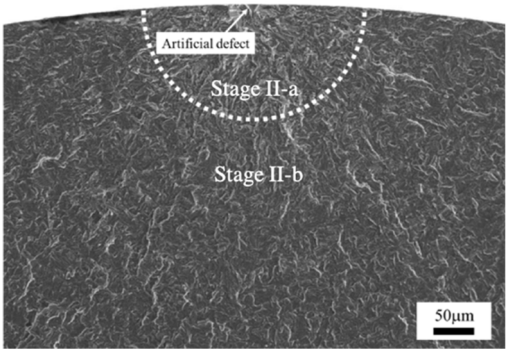

c. 10^{-2} Pa

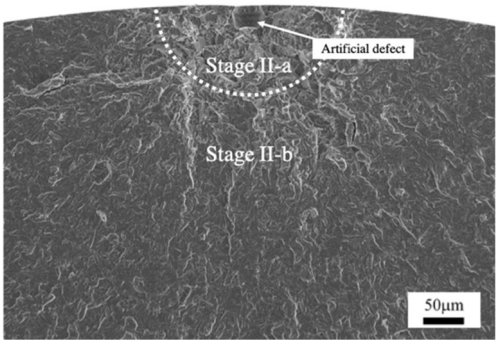

d. 10^{-6} Pa with excimer defect [16]

Fig. 10 Fracture surface image at low magnification in various environments. The different textures regarding Stage II-a and Stage II-b are separated by the dashed line.

4.2 Fracture surfaces at high magnification

4.2.1 Stage II-a region

Fig. 11 shows the high magnification of fracture surfaces of Stage II-a for various values of vacuum pressure. Regardless of the vacuum pressure, all of the fracture surfaces exhibit an uneven feature. The angular feature with sharp edges could be observed in air and 10^0 Pa, which is highlighted by the white arrows. In contrast, the surfaces with rounded edges and granular region were confirmed in 10^{-2} Pa and 10^{-6} Pa, and was also marked by the white arrows. Moreover, the granular and rounded feature was more remarkable in 10^{-6} Pa than in 10^{-2} Pa. Wanhill et al. has also reported that the round fracture surface feature is more remarkable in vacuum environments than that in air [35].

The 3D profile of the angular and granular features observed on the fracture surface were measured along lines A and B (shown in **Fig. 11 a** and **d**) by using the 3D measurement function of SEM. The resolution of 3D analysis is 50 nm/pixel so that it is sufficient to accurately reflect the texture of the microscopic fracture surface. As for the angular feature in air (**Fig. 12 a)**, the sharp edges were apparently identified at points ① and ②. Furthermore, the profile exhibits a relatively smooth texture where the altitude changes at the range indicated by ③. On the contrary, in the case of the granular feature shown **in Fig. 12 b**, small convex-concave particles (less than 1 μm) can be found, such as ④ and ⑤. Moreover, the texture in granular feature (⑥) is usually rougher than that in the angular feature shown at ③. The formation mechanism of the granular feature will be discussed in **Section 5.2**.

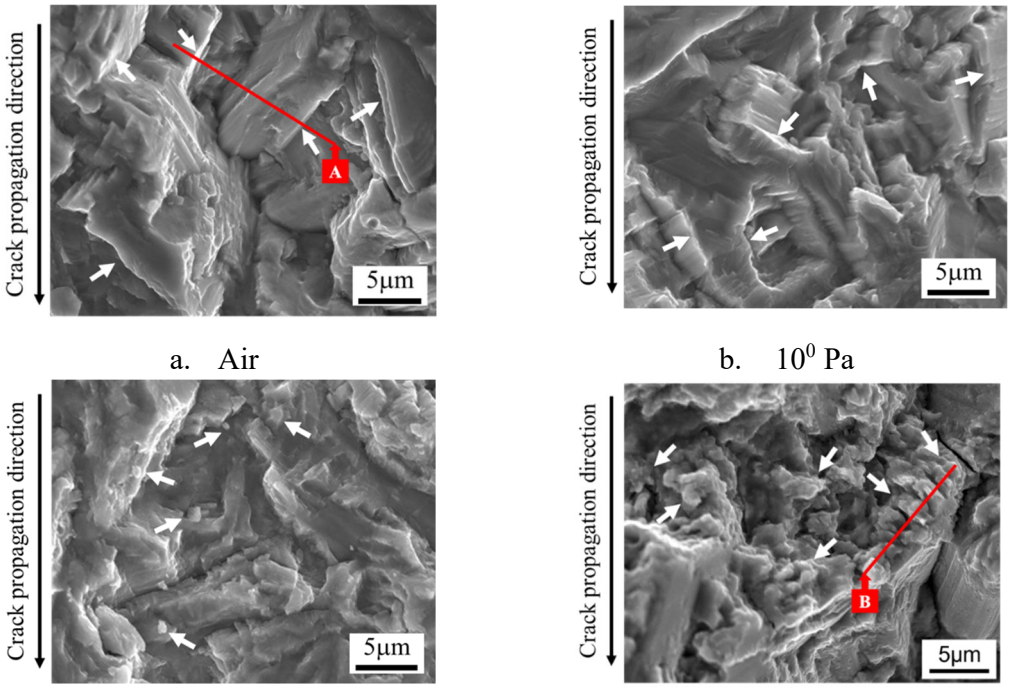

a. Air b. 10^0 Pa

c. 10^{-2} Pa d. 10^{-6} Pa

Fig. 11 Fracture surface at Stage II-a (ΔK = 6 MPa√m) in various environments. The angular feature with sharp edges in Fig. 11 a, b and the granular feature with rounded edges in Fig. 11 c, d are highlighted by the white arrows.

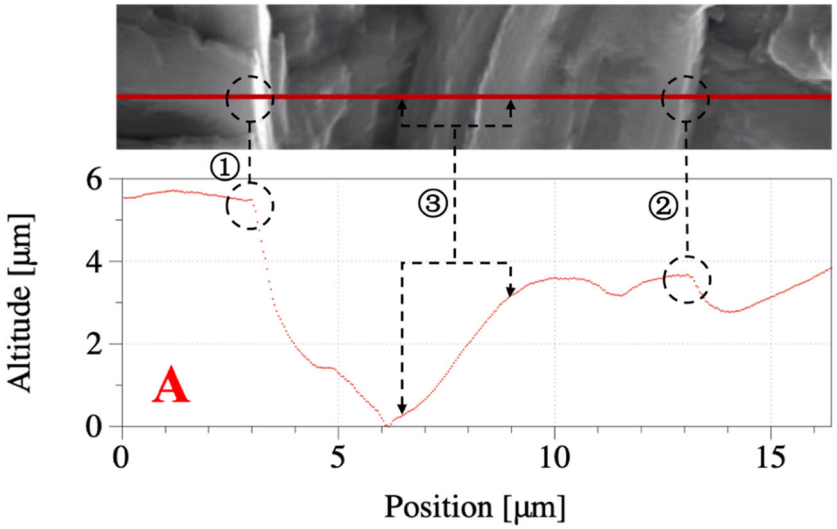

a. Angular feature in air

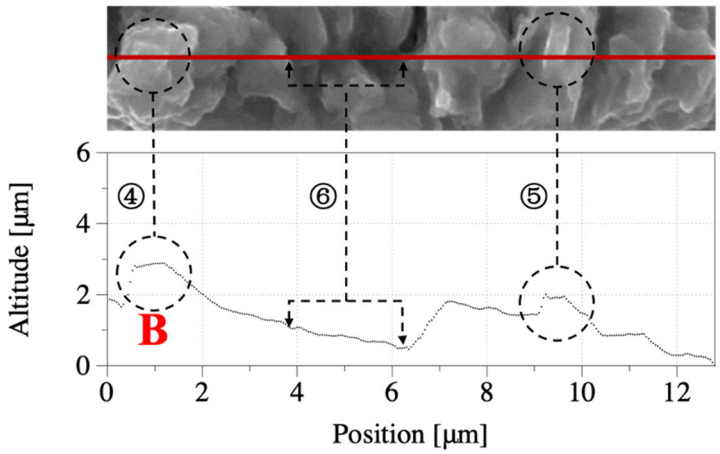

b. Granular feature in 10^{-6} Pa

Fig. 12 3D profiles of selected locations in air and 10^{-6} Pa.

4.2.2 Stage II-b region

Fig. 13 and **Fig. 14** exhibit the fracture surfaces at Stage II-b in air, 10^{0} Pa, and 10^{-2} Pa, 10^{-6} Pa. Focusing on images shown in **Fig. 13 a, c** and **Fig. 14** compared with the fracture surfaces in Stage II-a (**Fig. 11**), the surfaces are observed to have a flatter feature in Stage II-b. In addition, the feature variations in each environment in Stage II-b were not as obvious as those in Stage II-a. Focusing on magnified images at ΔK = 18 MPa√m, in the cases of both the air and 10^{0} Pa environments, the striation pattern shown in **Fig. 13 b** and **d** was observed at the flat region framed by the dashed rectangle in **Fig. 13 a** and **c**. The distances between the two striations (striation spacing) were measured for five times for each environment. As a result, the average striation spacing at ΔK = 18 MPa√m was 1.47×10^{-7} m with a standard deviation 3.84×10^{-8} m for air, and 1.29×10^{-7} m with a standard deviation 2.64×10^{-8} m for 10^{0} Pa, respectively. These striation spacings roughly matched with the crack growth rates shown in **Fig. 7**. In contrast, according to **Fig. 14**, the flat fracture regions at ΔK = 18 MPa√m in 10^{-2} Pa and 10^{-6} Pa shown by white arrows exhibited a rugged feature without any clear striation pattern.

The observation results are collated in **Table 5**. In summary, the similarities between the surface feature and the striation pattern were observed in between air and 10^0 Pa. The similarities between the surface feature and the lack of the striation pattern have also been confirmed between 10^{-2} Pa and 10^{-6} Pa. In the Stage II-a region, the granular feature became more pronounced, and the edges became rounder with a decrease of vacuum pressure. In the case of Stage II-b, the fracture surfaces under various vacuum pressures did not show a distinctive difference when compared to those in Stage II-a, which indicates that the vacuum environment had stronger effects on Stage II-a than Stage II-b.

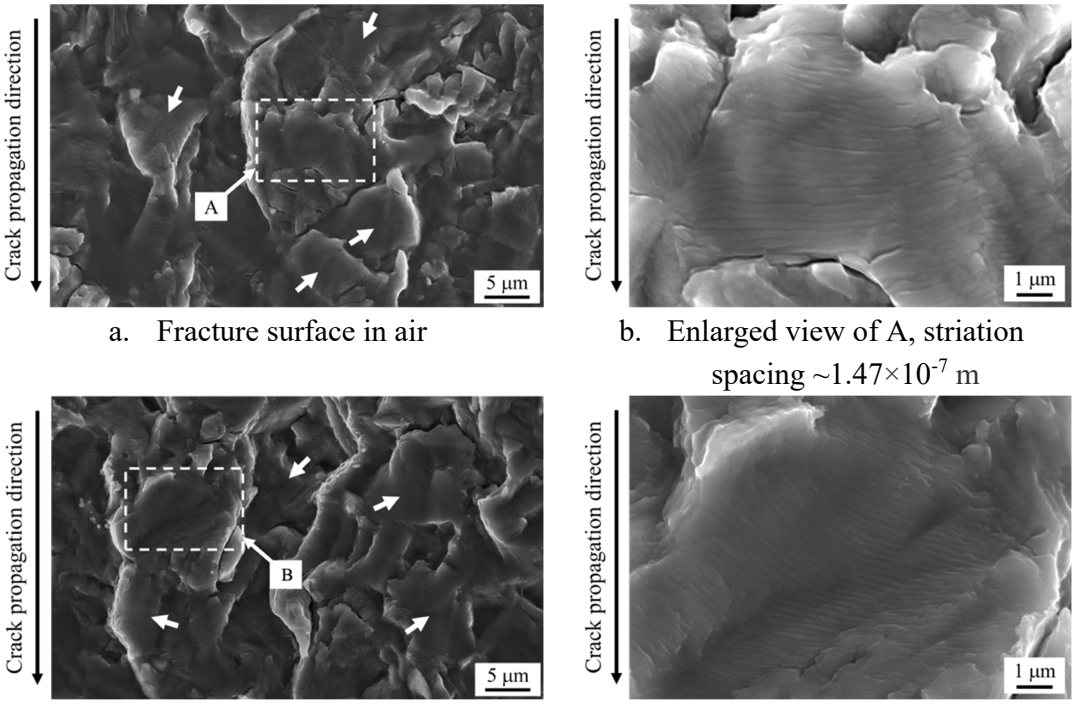

a. Fracture surface in air

b. Enlarged view of A, striation spacing ~1.47×10^{-7} m

c. Fracture surfaces in 10^0 Pa

d. Enlarged view of B, striation spacing ~1.29×10^{-7} m

Fig. 13 Fracture surfaces at Stage II-b (ΔK = 18 MPa$\sqrt{\text{m}}$) in air and 10^0 Pa. The striation pattern is marked by the white arrows.

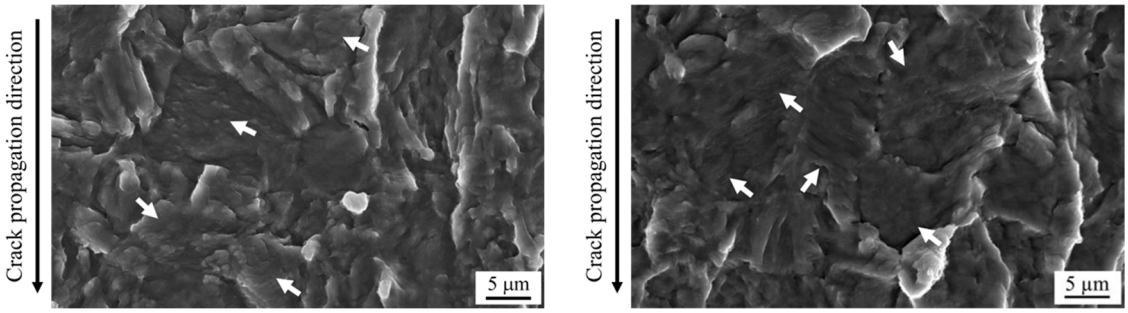

a. Fracture surfaces in 10^{-2} Pa b. Fracture surfaces in 10^{-6} Pa [16]

Fig. 14 Fracture surfaces at Stage II-b (ΔK = 18 MPa$\sqrt{m}$) in 10^{-2} and 10^{-6} Pa. The rugged feature without any clear striation pattern is shown by the white arrows in the flat region.

Table 5 Fracture surface feature.

Test atmosphere	Stage II-a		Stage II-b
	Fracture surface	Edge	Flat region
Air	Angular	Sharp	Striation
10^{0} Pa	Angular	Sharp	Striation
10^{-2} Pa	Less Granular	Less Round	Rugged
10^{-6} Pa	More Granular	More Round	Rugged

5. Discussion

5.1 Effects of vacuum pressure on crack propagation mechanism based on gas chemical adsorption

This study confirmed that the crack propagation rate in vacuum was lower than that in air. Many studies have already investigated the slow-down mechanism of crack propagation in vacuum. Duquette et al. explained that the formation of an adsorbed gas layer is suppressed at the nascent crack surface in vacuum [36]. In other words, cracks can propagate easily in the atmosphere owing to a decrease in surface energy. This effect is slow in vacuum; thus, crack propagation is relatively suppressed. Sugano et al. reported that the dislocation of the material is hindered by the adsorbed gas layer. Thus, plastic deformation is more likely to occur at the crack tip in vacuum than in the atmosphere. These phenomena can lead to an increase in the apparent resistance of crack growth due to plasticity-induced crack closure

[26]. Shyam et al. reported that slip reversibility, which also slows crack propagation, increases in vacuum owing to the lack of an adsorbed gas layer [37]. As mentioned above, suppressing the decrease in surface energy, plasticity-induced crack closure, accelerated plasticity, and slip reversibility due to the lack of adsorbed gas layer are considered the possible mechanisms for slow crack growth in vacuum. These mechanisms can also contribute to round and ductile fracture surface in a high-vacuum environment, as described in **Section 4.2**. Consequently, it is obvious that gas chemical adsorption, such as the oxidization process, should be one of the dominant reasons for the distinct crack propagation behavior in air and vacuum.

Moreover, the cracks exhibited distinct behaviors under various vacuum pressures in this study. One of the differences under various vacuum pressures is the number of gas molecules, which is a relevant factor when controlling the oxidization reaction. According to the kinetic theory of gases, as the number of gas molecules decreases, the incidence of gas molecules on the rupture surface also decreases, which results in the need for a longer period to form a monolayer. To calculate the time that is sufficient to form a monolayer based on the air pressure, the formula that was applied is given in **Eq**. (3) [38].

$$t_{\mathrm{m}} = \frac{N_{\mathrm{m}}\sqrt{2\pi mkT}}{p}, \tag{3}$$

where t_{m} is the time taken to form a monolayer, N_{m} is the maximum number of adsorbable molecules per unit area, m is the weight of the gas molecule. k is the Boltzmann's constant, T is the temperature, and p is the gas pressure. Assuming that the titanium alloy Ti-6Al-4V only oxidizes with oxygen in air, the gas molecule weight m and the gas pressure p in **Eq**. (3) employed the oxygen molecule weight and the partial pressure of oxygen in the atmosphere, respectively. As a result, the time to form a monolayer in air, 10^{0} Pa, 10^{-2} Pa, 10^{-4} Pa, and 10^{-6} Pa is approximately 10^{-8} s, 10^{-4} s, 10^{-2} s, 10^{0} s, and 10^{2}

s, respectively. In this study, the test frequency was set up at 60 Hz, which means that there was a window of about 10^{-2} s to form a monolayer during each load cycle. In other words, the window under 60 Hz is sufficient to form a complete monolayer in air and 10^{0} Pa, which explains the similarity in the crack propagation rate and the fracture surface between air and 10^{0} Pa. In contrast, the time was not adequate to form a complete monolayer in the case of 10^{-2} Pa, 10^{-4} Pa, and 10^{-6} Pa. This could be the reason that the decrease of the crack propagation rate with vacuum pressure was generally observed when the pressure was below 10^{-2} Pa. Meanwhile, in spite of the granular features that were formed below 10^{-2} Pa, their different significances between 10^{-2} Pa and 10^{-6} Pa also reflected the conclusion. Consequently, the effect of vacuum pressures on crack propagation depends on the time to form a surface coverage, which is determined by the testing frequency and the vacuum pressure.

5.2 Comparison with internal cracks and surface cracks in various pressures

As mentioned in **Section 1**, it is considered that the internal cracks propagate in a vacuum-like environment. However, it is very difficult to directly measure the vacuum pressure around internal cracks. In this section, to estimate the working environment around internal cracks, a comparison between internal cracks and surface cracks under various vacuum pressures will be discussed from two perspectives: crack propagation rate and granular fracture surface.

In our previous study, the crack growth rate of internal cracks in the same Ti-6Al-4V used in the present research was successfully measured using synchrotron radiation μ-CT imaging. This experiment was conducted at the third-generation large scale synchrotron radiation facility SPring-8, which is located in Hyogo, Japan, and the details are shown in the literature [39, 40]. The internal crack growth rate

measured by μ-CT is plotted in **Fig. 15** as a cross symbol, with the surface crack propagation rates under various pressures obtained in **Section 3**. For all of the rates of internal cracks, the values were below the lattice spacing (10^{-10} m/cycles), and they were significantly lower than those in air, 10^{0} Pa, and 10^{-2} Pa. However, there is a good agreement with the rate in 10^{-4} Pa and 10^{-6} Pa in the low ΔK regime around 5–8 MPa√m. This result indicates the possibility that the environment around internal cracks is similar to that for a high vacuum (≈10^{-4} Pa –10^{-6} Pa).

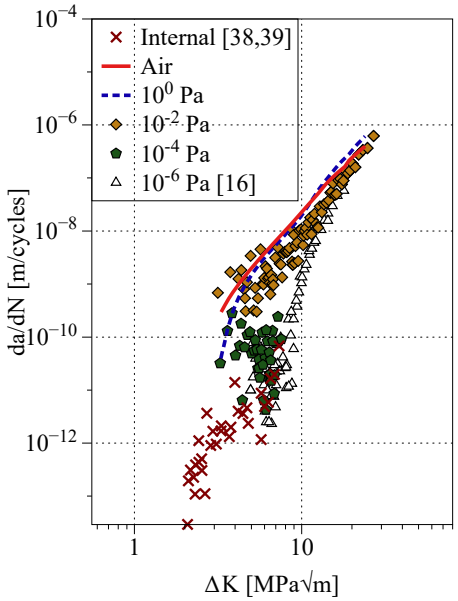

Fig. 15 Comparison between da/dN and ΔK with internal crack [38, 39] and surface crack in all test conditions.

However, internal and surface cracks in a high vacuum exhibit similar characteristics on fracture surfaces. **Fig. 16** exhibits the fracture surface of an internal fatigue fracture having the same material used in this study. This image was obtained by a uniaxial fatigue test under R=0.1 with a frequency of 120 Hz [3]. Similar to **Section 4.1**, **Fig. 16 a** shows that the bright and rough texture near the crack initiation site can be easily differentiated from the dark region in the high ΔK regime, and the boundary of the bright region is represented by the dashed line. This texture change corresponds to the transition from Stage II-

a to Stage II-b. The significant granular feature of internal cracks, which is similar to the fracture surface feature in 10^{-2} Pa and 10^{-6} Pa, was clearly observed in Stage II-a, as shown in **Fig. 16 b**.

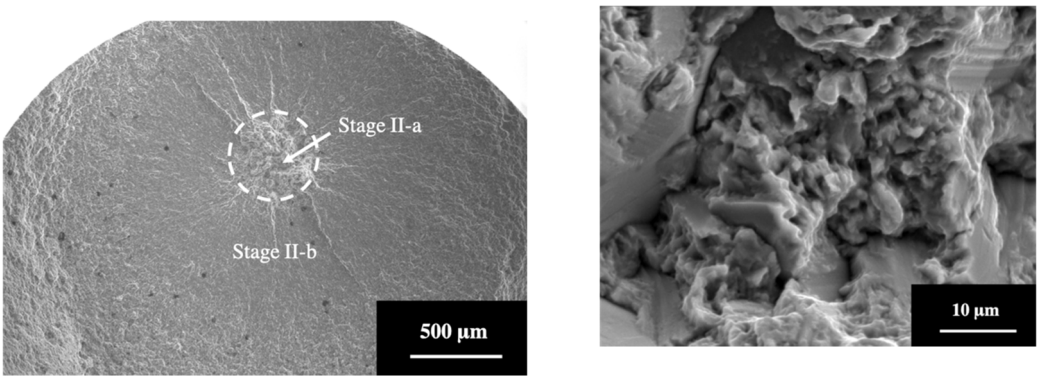

a. Low-magnification image

b. Granular feature in Stage II-a at high magnification image.

Fig. 16 Fracture surface image of an internal crack in Ti-6Al-4V (R = 0.1, σ_{max}= 600 MPa, f = 120 Hz).

The mechanism responsible for the granular region commonly observed at the internal crack initiation site has attracted much attention from VHCF researchers. Oguma et al. proposed that the micrometer concave-convex particles and microstructure refinement layer were presumably formed by the cold-welding during repeated surface contacting in Ti-6Al-4V, and the vacuum environment would promote the process of cold-welding [17]. Chang et al. employed numerous cyclic pressing (NCP) to create the nanograin layer near the crack initiation region in Ti-6Al-4V, and they reported the significance of the NCP process on microstructure refinement [41]. The positive stress ratio R=0.1 was applied in the present study both for surface cracks in vacuum and for the internal crack shown in **Fig. 16**; however, partial contacts can be achieved between upper and lower crack surfaces [17] owing to an increased closure level in a vacuum-like environment [26]. In addition, the granular feature of the internal crack was more similar to that in 10^{-6} Pa (**Fig. 11 d**). By combining these results and the similarity between the growth rate of internal cracks and surface cracks in vacuum, we can conclude that the internal crack

propagation process is strongly affected by its special environment, which is similar to a high vacuum level around 10^{-4} Pa – 10^{-6} Pa.

6. Conclusions

To clarify the effect of various pressures on the small crack propagation of Ti-6Al-4V, crack propagation tests were carried out using an hourglass shape specimen in air, 10^{0} Pa, 10^{-2} Pa, and 10^{-4} Pa for comparison with our previous results obtained under 10^{-6} Pa [16]. An artificial defect was created using a picosecond laser on each specimen surface to activate the small crack propagation. After being fractured, fractography was conducted to investigate in more detail the crack propagation behavior. Finally, the fracture surface of internal cracks was also compared with those in various environments to estimate the pressure around internal cracks in Ti-6Al-4V. The major results are as follows:

1. The crack propagation rates in air and 10^{0} Pa were similar. However, for 10^{-2} Pa, 10^{-4} Pa, and 10^{-6} Pa, the crack propagation rates became less than those in air and 10^{0} Pa. As the vacuum pressure decreased, the crack propagation rates decreased. The difference in the propagation rate affected by various vacuum pressures became more significant with the decrease of ΔK. The increase of the surface energy, plasticity and the slip reversibility in vacuum can appropriately explain this slowdown phenomenon on crack growth.
2. According to the fracture surface images at Stage II-a, an uneven surface was first observed in all environments. Then, an angular feature with sharp edges was observed in air and 10^{0} Pa. However, in the case of 10^{-2} Pa and 10^{-6} Pa, a granular feature with rounded edges was recognized, and it was more significant for 10^{-6} Pa. On the other hand, from the images at Stage II-b, all of the surfaces showed a

smoother feature than that in Stage II-a. The striation pattern was confirmed both in air and 10^0 Pa, whereas it was not clearly recognized in 10^{-2} Pa and 10^{-6} Pa. Further, the differences in the fracture surface under various vacuum pressures were more obvious in Stage II-a than in Stage II-b. With the similar result in conclusion 1, it was confirmed that there was a greater vacuum effect in Stage II-a compared with Stage II-b.

3. According to conclusions 1 and 2, the similarities of the crack propagation rate and the fracture surface were confirmed between air and 10^0 Pa, and they were also confirmed between 10^{-2} Pa and 10^{-6} Pa. The kinetic theory of gases was applied to explain this phenomenon, and based on the results, the window to form a monolayer was sufficient for air and 10^0 Pa under 60 Hz. In contrast, no sufficient time was provided in between 10^{-2} Pa and 10^{-6} Pa.
4. The internal crack behaviors were compared with those of surface cracks in various pressures. The propagation rate of internal cracks exhibited good agreement with surface cracks in 10^{-4} Pa and 10^{-6} Pa, which was much lower than that in air and low vacuum. From the perspective of the feature of fracture surfaces, a similar granular feature was observed in the internal crack and surface cracks whose test pressures were below 10^{-2} Pa. These indicate that the vacuum environment was one of the dominant factors responsible for the growth slowdown behavior and the formation of granular features in internal cracks. In addition, it could be concluded that the internal cracks in Ti-6Al-4V were likely to propagate in a high vacuum level.

Acknowledgement

The authors acknowledge the support of a Grant-in-Aid for JSPS Fellows (16J01058) and for Scientific Research (A, 2018, 18H03748) from the Japan Society for the Promotion of Science, Japan. The authors are profoundly grateful to the graduate student at Hokkaido University, Mr. Yusuke Kobayashi for his technical support to the experiment.

Reference

[1] Marines I, Bin X, Bathias C. An understanding of very high cycle fatigue of metals, International Journal of Fatigue. 2003;25:1101-7.

[2] Pyttel B, Schwerdt D, Berger C. Very high cycle fatigue–Is there a fatigue limit?. International Journal of fatigue. 2011;33:49-58.

[3] Oguma H, Nakamura T. The effect of microstructure on very high cycle fatigue properties in Ti-6Al-4V. Scripta Mater. 2010;63:32-4.

[4] Neal DF, Blenkinsop PA. Internal fatigue origins in α-β titanium alloys. Acta Mater 1976;24(1):59–63.

[5] Atrens A, Hoffelner W, Duerig TW, Allison JE. Subsurface crack initiation in high cycle fatigue in Ti-6Al-4V and in a typical stainless steel, Scr Mater, 1983;17(5):601–6.

[6] Nalla RK, Boyce BL, Campbell JP, Peters, JO, Ritchie RO. Influence of microstructure on high-cycle fatigue of Ti-6Al-4V: Bimodal vs. lamellar structures. Metall Mater Trans A. 2002;33(3):899–918.

[7] McEvily AJ, Nakamura T, Oguma H, Yamashita K, Matsunaga H, Endo M. On the mechanism of very high cycle fatigue in Ti-6Al-4V, Scripta Mater, 2008;59(11):1207-9.

[8] Heinz S, Balle F, Wagner G, Eifler D. Analysis of fatigue properties and failure mechanisms of Ti6Al4V in the very high cycle fatigue regime using ultrasonic technology and 3D laser scanning vibrometry, Ultrasonics, 2013;53(8):1433-40.

[9] Liu X, Sun C, Hong Y. Faceted crack initiation characteristics for high-cycle and very-high-cycle fatigue of a titanium alloy under different stress ratios. Int J Fatigue, 2016;92:434-441.

[10] Pan X, Su H, Sun C, Hong Y. The behavior of crack initiation and early growth in high-cycle and very-high-cycle fatigue regimes for a titanium alloy. Int J Fatigue. 2018;115:67-78.

[11] Liu X, Sun C, Hong Y. Effects of stress ratio on high-cycle and very-high-cycle fatigue behavior of a Ti-6Al-4V alloy. Mater Sci Eng A. 2015;622:228-35.

[12] Nakamura T, Oguma H, Shiina T. Influential factors on interior-originating fatigue fractures of Ti-6Al-4V in gigacycle region: focusing on stress ratio and internal environment of material. In: Lüetjering G, Albrecht J, eds. Ti-2003 Science and Technology, Wheinheim: Wiley-VCH; 2004:1775–82.

[13] Benedetti M, Fontanari V, Bandini M, Savio E. High- and very high-cycle plain fatigue resistance of shot peened high-strength aluminum alloys: The role of surface morphology. Int J Fatigue. 2015;70:451-62.

[14] Nishijima S, Kanazawa K. Stepwise S-N curve and fish-eye failure in gigacycle fatigue. Fatigue Fract Eng M. 1999;22:601-7.

[15] Nakamura T, Oguma H, Shinohara Y. The effect of vacuum-like environment inside sub-surface fatigue crack on the formation of ODA fracture surface in high strength steel. Procedia Eng. 2010;**2**:2121–29.

[16] Yoshinaka F, Nakamura T, Takaku K. Effects of vacuum environment on small fatigue crack propagation in Ti-6Al-4V. Int J Fatigue. 2016:29–38.

[17] Oguma H, Nakamura T. Fatigue crack propagation properties of Ti-6Al-4V in vacuum environments. Int J Fatigue 2013;50:89–93.

[18] Yoshinaka F, Nakamura T. Effect of vacuum environment on fatigue fracture surfaces of high strength steel. Mech Eng Lett. 2016;2:15-00730.

[19] Hénaff G, Odemer G, Tonneau Morel A. Environmentally assisted fatigue crack growth mechanisms in advanced materials for aerospace applications. Int J Fatigue. 2007;29:1927-40.

[20] Karr U, Schönbauer B M, Mayer H. Near-threshold fatigue crack growth properties of wrought magnesium alloy AZ61 in ambient air, dry air, and vacuum. Fatigue & Fracture of Engineering Materials & Structures. 2018;41(9):1938-47.

[21] Snowden K. U. The effect of atmosphere on the fatigue of lead. Acta Metallurgica. 1964;12(3):295-303.

[22] Endo K, Komai K. Fatigue crack growth of aluminum alloy in ultra-high vacuum. J. Soc. Mater. Sci. Jpn.. 1977;26(281):143-8.

[23] M. Gao, P. S. Pao, R. P. Wei. Chemical and Metallurgical Aspects of Environmentally Assisted Fatigue Crack Growth in 7075-T651 Aluminum Alloy. Metallurgical Transactions A. 1988;19:1739-50.

[24] Jha S K, Szczepanski C J, Golden P J, et al. Characterization of fatigue crack-initiation facets in relation to lifetime variability in Ti-6Al-4V. International journal of fatigue. 2012;42:248-257.

[25] Nisitani H. Stress intensity factor for a semi-elliptic surface crack in a shaft under tension. Transactions of the Japan Society of Mechanical Engineers, Series A. 1984;50(453):1077-83.

[26] Sugano M, Kanno S, Satake T. Fatigue behavior of titanium in vacuum. Acta Metall. 1989;37(7):1811-20.

[27] Shen, H, S. E. Podlaseck, I. R. Kramer. Effect of vacuum on the fatigue life of aluminum. Acta Metallurgica. 1966;14(3):341-6.

[28] Furuya Y. A new model for predicting the gigacycle fatigue strength of high-strength steels. Materials Science and Engineering: A. 2019;743:445-452.

[29] Furuya Y. Small internal fatigue crack growth rate measured by beach marks. Materials Science and Engineering: A. 2016;678:260-6.

[30] Forsyth, P J E. Fatigue damage and crack growth in aluminium alloys. Acta Metallurgica. 1963;11(7):703-715.

[31] Birkbeck G, A. E. Inckle, G. W. J. Waldron. Aspects of Stage II fatigue crack propagation in low-carbon steel. Journal of Materials Science. 1971;6(4):319-323.

[32] Totten G. Fatigue crack propagation. Advanced Materials and Processes. 2008;166(5):39.

[33] Grinberg N M. The effect of vacuum on fatigue crack growth. International Journal of Fatigue. 1982;4(2):83-95.

[34] Paris P, Erdogan F. A critical analysis of crack propagation laws. 1963;528-533.

[35] Wanhill R.J.H. Material-based failure analysis of the Lynx-282 rotor hub. NLR Contract Report NLR-CR-99189, National Aerospace Laboratory NLR, Amsterdam, The Netherlands. 1999.

[36] Duquette DJ, Gell M. The effect of environment on the mechanism of Stage I fatigue fracture. Metallurgical and Materials Transaction B. 1971;2:1325-31.

[37] Shyam A, Milligan W. A model for slip irreversibility, and its effect on the fatigue crack propagation threshold in a nickel-base superalloy. Acta Materialia. 2005;53:835-44.

[38] Jousten K. Handbook of vacuum technology. Wiley & Sons. 2016.

[39] Yoshinaka F, Nakamura T, Nakayama S, et al. Non-destructive observation of internal fatigue crack growth in Ti-6Al-4V by using synchrotron radiation μCT imaging. International Journal of Fatigue. 2016;93:397-405.

[40] Yoshinaka F, Nakamura T, Takeuchi A, Uesugi M, Uesugi K. Initiation and growth behavior of small internal fatigue cracks in Ti-6Al-4V via synchrotron radiation microcomputed tomography. Fatigue Fract Eng Mater Struct. 2019;42:2093–2105.

[41] Chang Y, Pan X, Zheng L, et al. Microstructure refinement and grain size distribution in crack initiation region of very-high-cycle fatigue regime for high-strength alloys. International Journal of Fatigue, 2020;143:105473.